

Structural, optical and DC conduction studies on vacuum evaporated Sr doped BaTiO₃ (BST) thin films prepared from Sr doped BaTiO₃ nano particles

R. SENGODAN^a, B. CHANDAR SHEKAR^{b*}

^aDepartment of Physics, Kumaraguru College of Technology, Coimbatore, Tamil Nadu, India

^bDepartments of Physics, Kongunadu Arts and Science College, G.N- Mills, Coimbatore, Tamil Nadu, India

Barium titanate (BaTiO₃) doped with Strontium (BST) nanoparticles prepared by using wet chemical method were thermally evaporated on to well cleaned glass substrates under the vacuum of 2×10^{-5} torr, using 12A4 Hind Hivac coating unit. The structure, optical and electrical properties of the deposited BST thin films were studied using the X-ray diffraction (XRD), optical transmittance and current-voltage measurements. The thickness of the film was measured by quartz crystal monitor. From X-ray analysis, it has been found that BaTiO₃ nanoparticles possess tetragonal structure and the deposited films were polycrystalline in nature, whereas the crystallinity increases with increase of thickness. The extinction coefficient of the BST thin films decreases and on the other hand, refractive index increases with increasing thickness. The optical band gap energy value decreases with increase of film thickness. In the DC conduction studies, the Current-Voltage characteristics of the films showed ohmic conduction in the low field region. The conduction mechanism was found to be Poole-Frenkel at high field region. The activation energy values were estimated and were found to be decreasing with increasing applied field. The zero field value of the activation energy was found to be 0.28 eV.

(Received August 12, 2013; accepted May 15, 2014)

Keywords: Barium strontium titanate, Thermal evaporation, XRD, UV – Visible, DC Conduction and Poole – Frenkel

1. Introduction

In recent years barium strontium titanate (BST) thin films have received intensive research interest for their device applications, such as bolometers [1, 2], gas sensor [3], non-volatile memory, optoelectronic device, tunable microwave filters [4] and radio-frequency microelectromechanical (RF-MEMS) capacitive switches [5]. Due to the desirable properties and applications, over the last few decades, synthesis of BST nanoparticles and thin film has attracted great attention. Most of the experimental work carried out so far related to preparation of nanoparticles by polymeric precursor method [6], wet chemical method, co-precipitation, alkoxide hydrolysis [7], metal-organic processing [8], hydrothermal treatment [9] and the solid state reaction of mixed oxide route [10]. Among these methods, wet chemical method is a promising technique that offers relative low cost, uniform size and homogenous particles. Different techniques have been used to prepare thin film of BST such as sol – gel method [11], r.f. - sputtering [12], pulsed laser ablation [13], metal-organic chemical vapour deposition [14] and vacuum evaporation [15]. Among these methods vacuum evaporation is advantageous to obtain good quality of BST thin films. To the best of our knowledge, there are few reports on the optical properties and DC conduction studies of the BST thin films. Recently, Huang et al.

reported the infrared optical properties of Ba_{0.8}Sr_{0.2} TiO₃ thin films using ellipsometry [16]. Hu et al. reported the effect of film thickness on the infrared optical properties of the Ba_{0.9}Sr_{0.1}TiO₃ thin films [17]. Hence in this present paper we have discusses the structural, optical and electrical properties of vacuum evaporated BST thin films.

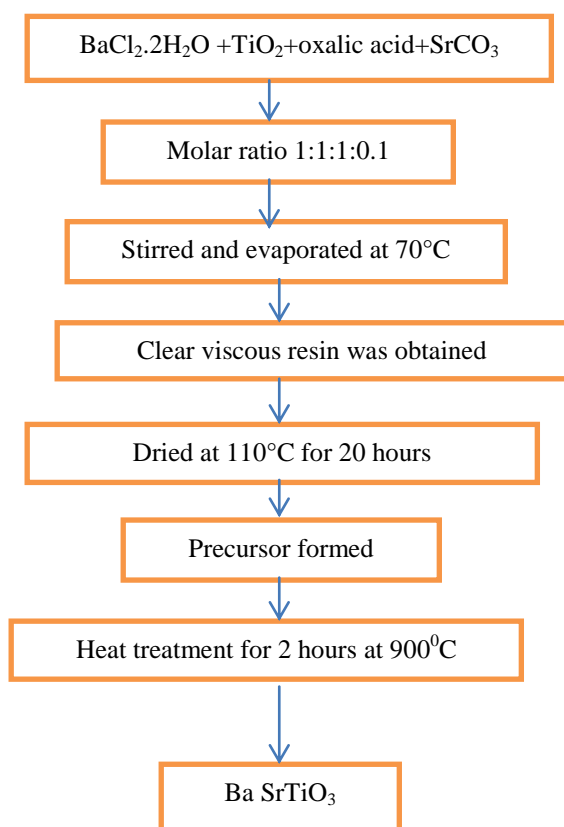
2. Experimental details

2.1 Synthesis of BaSrTiO₃ nanoparticles

BST nanoparticles were synthesized by using wet chemical method. The starting materials used were Barium chloride (BaCl₂.2H₂O), Titanium dioxide (TiO₂), Strontium carbonate (SrCO₃) and Oxalic acid. A solution of Ba: Ti: Oxalic acid: SrCO₃ having mole ratio 1: 1: 1: 0.1 was stirred and heated at 70°C till a clear, viscous resin was obtained and then dried at 110°C for 20 hours. The precursor formed was heated at 900°C for 2 hours to form BST nanoparticles. The chemical composition of our BST nanoparticles is follows



Sample preparation



2.2 BaTiO₃ thin film preparation

Using the conventional 12A4 Hind Hivac coating unit, pure (99.999%) aluminium was evaporated from a tungsten filament onto well-cleaned glass substrates through suitable masks to form the bottom electrode. Prepared BST nanoparticles were then evaporated from a molybdenum boat to form the dielectric layer. An aluminium counter electrode was evaporated onto the dielectric through suitable masks to complete the aluminium - BaTiO₃ - aluminium (metal-Insulator-metal structure) device. A working pressure of 2×10^{-5} torr was maintained in all the evaporation processes. For the structural and optical analysis, the BST films were deposited on the plane glass substrates.

2.3 Characteristics of BST nanoparticles and BST Thin films

Thickness of the films was measured through quartz crystal monitor ("Hind Hivac" Digital Thickness Monitor Model-DTM-101). The structural aspects of the particles and films were analyzed, using X-ray diffractometer with filtered CuK α radiation ($\lambda = 1.5418 \text{ \AA}$). The optical studies were carried out by using JASCO-UV/VISIBLE spectrophotometer (model UVIVDEC 610, Japan). The DC electrical measurement was performed at different applied voltages and at different temperatures. The current through the sample was recorded by Keithley instruments models

2611/2612. The temperature was recorded using a chromel-alumel thermocouple placed very close to the samples.

3. Result and discussion

3.1 X – Ray Diffraction Analysis

Fig. 1 shows the XRD pattern of BST nanoparticles. The XRD pattern of BST particles exhibited tetragonal structure, because the peak splitting was found clearly in the (002) plane, which shows its high degree of tetragonality [18- 20]. The average crystallite size (D) of the particle was calculated by using Scherrer's formula and it was found to be 40 nm.

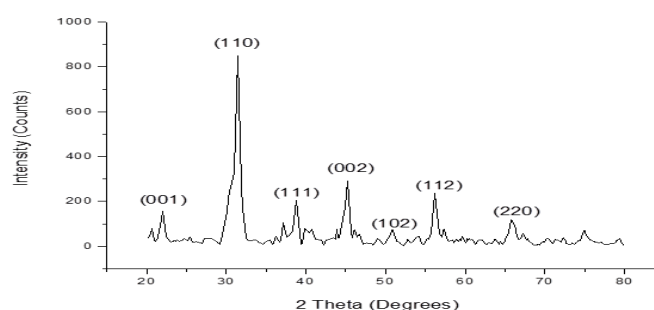


Fig. 1. XRD pattern of BST nanoparticles.

The crystallite size is calculated from the Scherrer's formula from the full width at half - maximum (FWHM) of the XRD peaks

$$D = 0.94\lambda / \beta \cos\theta \quad (1)$$

Where λ is the wavelength of the X-rays used, 2θ is the angle between the incident and scattered X-rays and β is the full width at half maximum. The strain (ϵ) is calculated from the formula

$$\epsilon = \beta \cos\theta / 4 \quad (2)$$

The dislocation density (δ) is defined as the length of dislocation lines per unit volume of the crystal and is given by

$$\delta = 1/D^2 \quad (3)$$

Fig. 2 shows the XRD patterns of the BST thin films deposited on glass substrate with different film thickness. The films were found to be polycrystalline with (001) (110), (111), (200), (102) and (112) orientation peaks arising at 2θ values of 23.95° , 30.30° , 36.84° , 43.06° , 52.64° and 56.63° respectively. The intensity of (110) peak was higher than (111) and (200) peaks. As can be seen, the crystallization of the films strongly depends on the film thickness. The intensity of the peak increases with increase in film thickness indicating improved crystallinity [21].

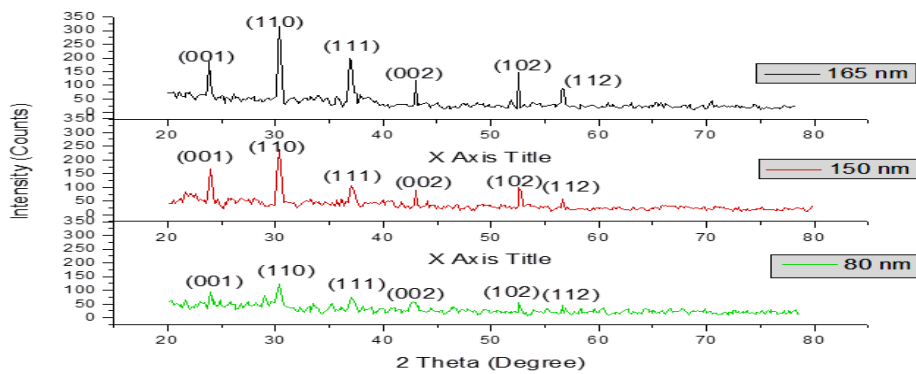


Fig. 1. XRD pattern of BST thin films of different thickness.

Table 1 shows the calculated values of crystallite size (D), dislocation density (δ) and strain (ϵ) for different thickness. From the table it has been observed that the grain size increases with increase in thickness whereas the strain and the dislocation density decrease with the increase in thickness. Due to the increase in crystalline size with film thickness, the defects in the lattice are decreased, which in turn reduce the internal micro strain and dislocation density/or the columnar grain growth is increased [22, 23].

Table 1. Structural parameters of BST thin films of different thicknesses.

Thickness (nm)	2 θ Degrees	hkl	Crystalline Size (D) nm	Strain (ϵ) $\text{lin}^{-2}\text{m}^{-4}$	Dislocation density (δ) $\times 10^{15} (\text{lin}/\text{m}^2)$
150	24.08	100	24.28	1.427	1.696
	32.66	101	26.23	1.320	1.453
	37.01	111	21.25	1.631	2.214
	45.14	002	20.31	1.706	2.426
	56.61	112	23.62	1.567	1.792
165	24.08	100	25.86	1.340	1.495
	32.66	101	28.45	1.218	1.235
	37.01	111	23.13	1.498	1.869
	45.14	002	20.69	1.673	2.336
	56.61	112	24.87	1.393	1.616

3.2 Optical properties

The transmittance spectra of the vacuum evaporated BST thin films of various thicknesses are presented in Fig. 3. It is seen that the transmittance decreases with the increase in the film thickness, which leads to a decrease in light scattering losses [24]. High transmittance in the higher wavelength region and a sharp absorption edge were observed in the films [25]. The average transmission value for the BST film is over 75%, which is higher than the transmittance of pure BaTiO_3 .

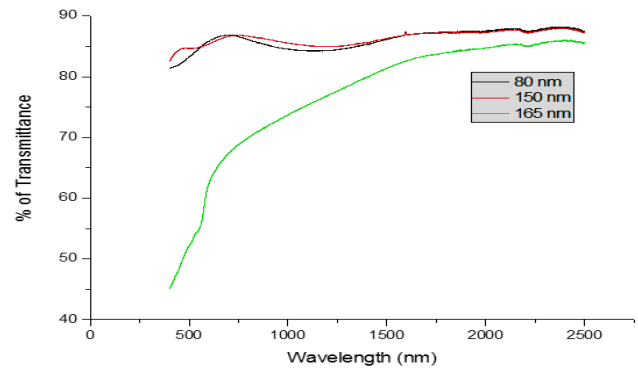


Fig. 3. The transmittance spectra of the BST thin films of different thickness.

From the transmittance spectra the Extinction coefficient (k) can be calculated from the relation,

$$k = 2.303\lambda \log(1/T_0)/4\pi d \quad (4)$$

Where d is the thickness of the film and λ wavelength of the light

Fig. 4 shows the variation of Extinction coefficient (k) with wavelength for BST films of different thicknesses. The value of extinction coefficient decreases with increase in film thickness, which may be due to the improvement in the crystallinity with the increase in film thickness leading to the minimum imperfections.

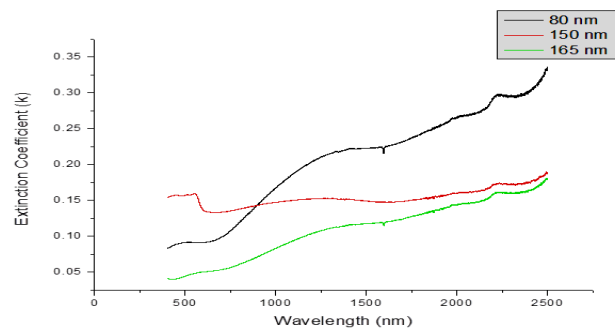


Fig. 4. The variation of Extinction coefficient (k) with wavelength for BST films of different thicknesses.

For direct allowed transition the absorption coefficient and photon energy are related by expression

$$\alpha h\nu = A (h\nu - E_g)^n \quad (5)$$

Where A is a constant and E_g the optical band gap energy. The $(\alpha h\nu)^2$ is plotted against the photon energy ($h\nu$) for BST films of various thicknesses and the energy gap for these films are obtained by extrapolating the linear straight line portion of the curve to the energy axis. All the plots show straight-line portions supporting the interpretation of direct band gap for all the films. From the plot, it is concluded that the optical transition in these films is direct and allowed. The variation of $(\alpha h\nu)^2$ versus photon energy

for BST thin film of different thicknesses is shown in Figs. 5, 6 and 7. It is observed that the band gap (E_g) decreases with increase in thickness as shown in Table 2. The decrease in band gap with increase in film thickness can be explained on the basis of island structure concept proposed by Neugebauer and Webb [26]. The decrease in optical band gap energy with increase in film thickness is due to the increased grain size of the higher thickness of the film (27). Hence, the variations of band gap in the films are supposed to be due to the changes in the lattice constants, which may arise because of the change in microstrain.

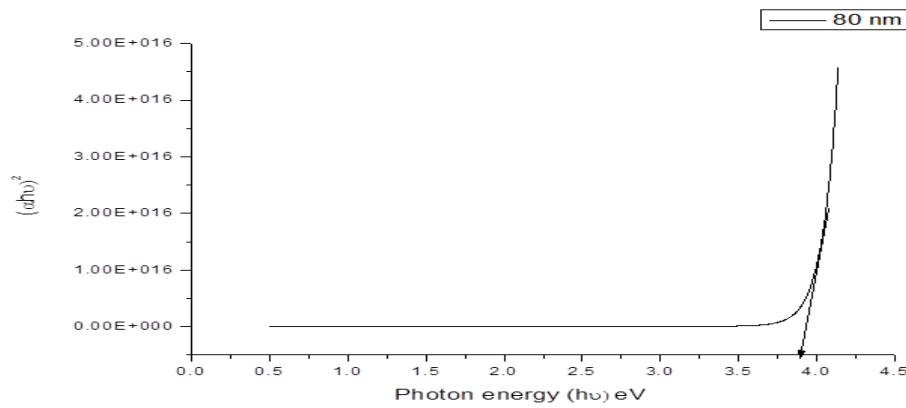


Fig. 5. The variation of $(\alpha h\nu)^2$ versus photon energy for BST thin film of thickness 80 nm.

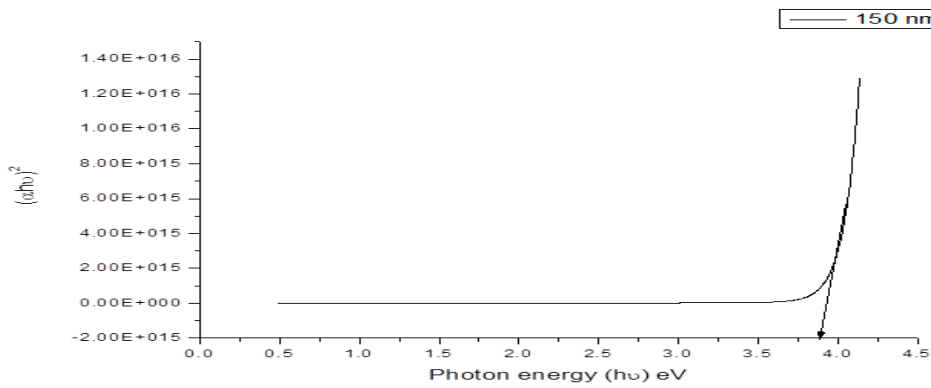


Fig. 6. The variation of $(\alpha h\nu)^2$ versus photon energy for BST thin film of thickness 150 nm.

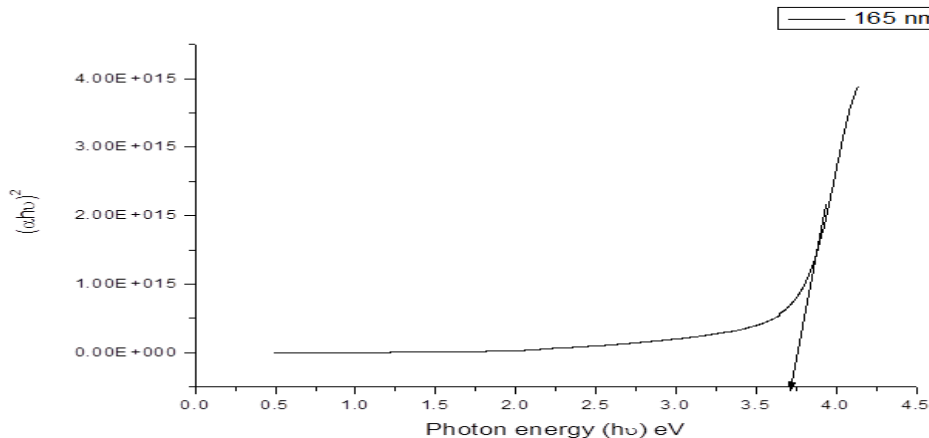


Fig. 7. The variation of $(\alpha h\nu)^2$ versus photon energy for BST thin film of thickness 165 nm.

Table 2. The band gap for different thicknesses of BST thin films.

Thickness (nm)	Band gap (eV)
80	3.9
150	3.88
165	3.74

Fig. 8 shows the Variation of refractive index with wavelength of BST thin films at different thickness. It is observed that refractive index of films increases with increase of thickness. This difference for the refractive index may be owing to both the crystalline quality of the films and packing density. XRD measurement show that the FWHM in BST thin films decreases with increasing thickness. However, the peak position does not shift with increasing thickness. According to Scherrer's equation, the average crystallite size is inversely proportional to the FWHM and can be calculated. The result indicates that the average crystallite size increases from 22.5 to 25.55 nm with an increasing thickness [28]. So the refractive index of the films increases with increasing crystallite size. The similar phenomenon for the BaTiO₃ thin films has been reported by Thomas et al [29].

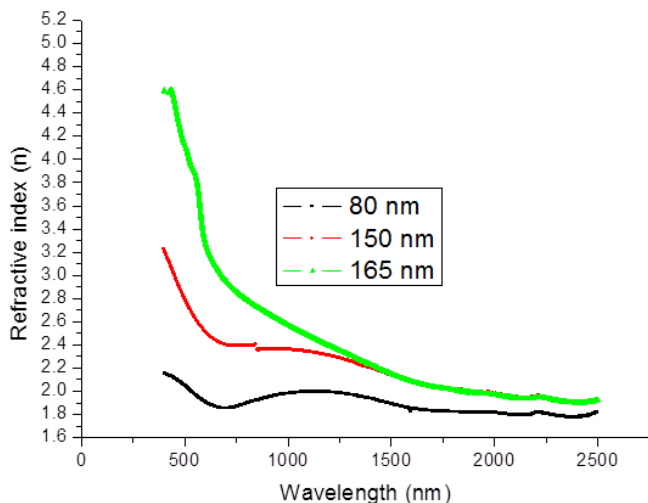


Fig. 8. Variation of refractive index with wavelength of BST thin films at different thickness.

3.3 D.C. conduction

The J-V characteristics measured at 303-448 K for BST thin film of thickness 150 nm is shown in Fig. 9. The J-V curves show two distinct regions corresponding to two different types of conduction. At very low applied voltages (<3V) the conduction process, due to thermally excited carriers, is Ohmic. As the applied voltage V is increased (>3V), the current I increases non-linearly. The non-Ohmic I-V dependence is usually interpreted in terms of space-charge limited currents [30] or as the hopping

process in thin films [31]. In the non-Ohmic region the observed slope is less than two, indicating the non-existence of the Space Charge Limited (SCL) conduction mechanism.

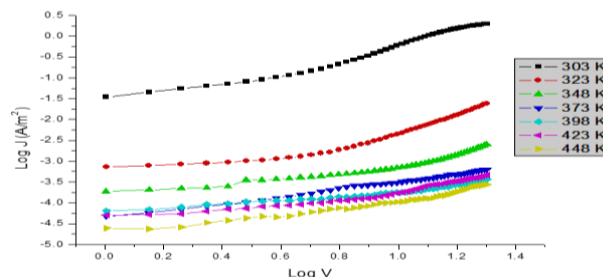


Fig. 9. J-V characteristics for BST thin films of thickness 150 nm.

The transition voltage, which separates the two regions, is found to be independent of temperature. The above result indicates that with the increase of temperature the probability of thermal ionization of the trapping centers increases, thus causing a shift in the quasi-Fermi level, which gives rise to a lowering of the barrier across which electrons have to be transported and the conduction becomes more or less Ohmic. The increase in current at high temperatures can be due to softening of the substance and because of this the injected charge carriers can drift more easily to the dielectric volume. This gives rise to a large current at high temperatures. At lower fields, the injection of carriers from the contact is less and the initial current is governed by the intrinsic free carriers in the materials. The current will be Ohmic until the injected free carrier density becomes comparable with the thermal carrier density.

Fig. 10 shows the dependence of logarithmic current with the square root of the applied voltage at different temperatures. The nature of these plots indicates that the conduction process is governed by a mechanism in which the charge carriers are released by thermal activation over a Coulombic potential barrier that is decreased by the applied electric field. The nature of such a barrier can be understood in two ways. The charge carriers (electrons) can cross over the barrier between cathode and dielectric, as is the case with Schottky emission, taking the image force into consideration. Alternatively, carriers can be released due to ionization of impurity centers in the dielectrics (Poole-Frenkel effect). In both the above processes there is a current-field relationship which is of the form

$$I \propto \exp \beta F^{1/2}$$

The restoring force in Richardson-Schottky (R-S) and Poole-Frenkel (P-F) effects is the Coulomb interaction between the escaping electron and positive charge. They differ in that positive image charge is fixed for P-F barriers but mobile for Schottky emission. This results in a barrier lowering twice as much for the P-F effect.

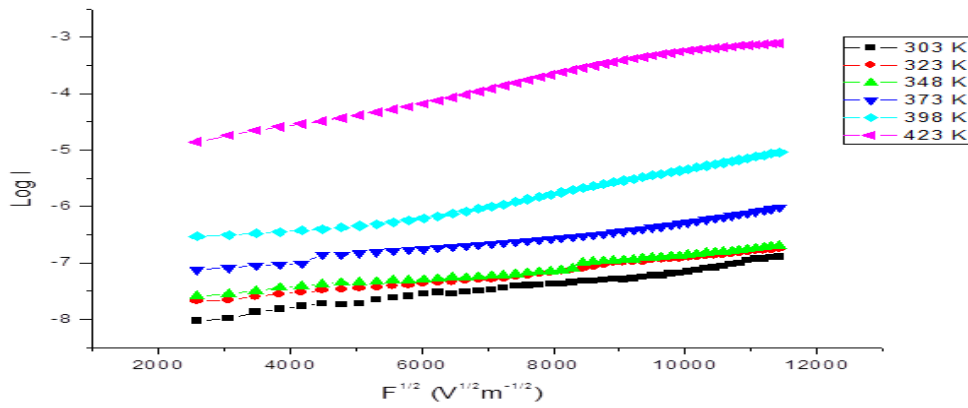


Fig. 10. Dependence of logarithmic current with the square root of the applied voltage at different temperatures of 150 nm thick film.

To determine the actual conduction mechanism, the value of the β -factor at different temperatures calculated from the slope of $\text{Log } I$ vs \sqrt{F} are compared with the theoretically calculated value of β assuming a particular mechanism to be operative. The theoretical values of β_{PF} can be obtained from the relationship

$$\beta_{PF} = 2\beta_{RS} = 2 \left[\frac{e}{4\pi\epsilon\epsilon_0} \right]^{1/2}$$

Where ϵ_0 is the permittivity of free space, ϵ dielectric constant and e the electronic charge.

The experimental and theoretical values of β for Richardson-Schottky and Poole-Frenkel mechanisms are shown in Table 3. The experimental values of β are in close agreement with the theoretically calculated values of β_{PF} . Hence, the P-F mechanism seems to be the governing mechanism in the present case [32].

Table 3. The experimental and theoretical values of β for Richardson-Schottky and Poole-Frenkel.

Temperature (K)	$\beta_{Exp} \times 10^{-5}$	$\beta_{Ther} \times 10^{-5}$	
		RS	PF
303	1.273		
323	0.899		
348	0.871	0.6416	1.282
373	1.48		
398	1.479		
423	1.282		

Fig. 11 shows the Arrhenius plots between $\text{Log } I$ vs $1000/T$ at different fields for BST film of thickness 150 nm. The activation energy values for the various fields calculated from these plots are given in the Table 4. The activation energy values decrease with the increasing applied field, suggesting that the potential barriers are lowered due to the applied field. The obtained results are in accordance with those of previous workers [33].

This suggests that the applied field interacts with the field of the ionizable centre so that the energy required for an electron to escape in a direction opposite to the field direction (i.e. in the field-assisted or 'forward' direction) is reduced by an amount. Zero field activation energy is estimated by extension of the line to reach the activation energy axis as in the Fig. 12 and found to be 0.28 eV [34].

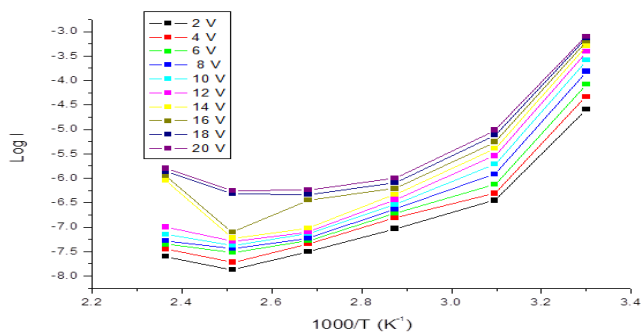


Fig. 11. Log I vs $1000/T$ at different fields for BST thin film of thickness 150 nm.

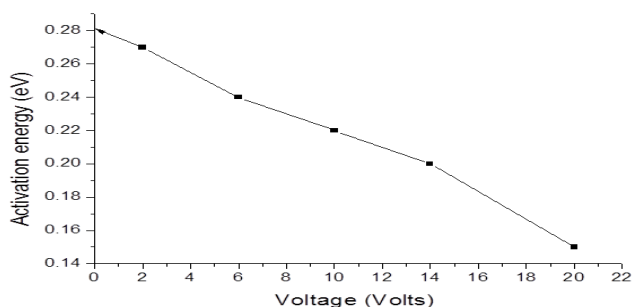


Fig. 12. Voltage Vs Activation Energy BST thin films of thickness.

Table 4. Activation energy for different voltages.

Voltage (Volts)	Activation energy (eV)
2	0.27
6	0.24
10	0.22
14	0.20
20	0.15

4. Conclusion

We have successfully synthesized nanoparticles of BST by low cost wet chemical method using commercially available chemicals such as oxalic acid, TiO_2 , $BaCl_2$, $SrCO_3$. Thin films of few hundred nanometre thickness was prepared on well cleaned glass plate for the first time using thermal evaporation method. X-ray analysis showed that particles have a tetragonal nature and the deposited films have a polycrystalline nature, whereas crystallinity increases with increasing thickness. In the D.C. conduction studies, Current-Voltage measurements showed Ohmic conduction at lower fields and Poole - Frenkel conduction at higher fields. The activation energy was determined and it was found to be decreasing with increase in applied voltage. The zero field activation energy was found to be 0.28 eV.

References

- [1] K. Hashimoto, H. Xu, T. Mukaigawa, R. Kubo, H. Zhu, M. Noda, M. Okuyama, *Sens. Actuata. A* **88**, 10 (2001).
- [2] M. Noda, H. Xu, T. Mukaigawa, H. Zhu, K. Hashimoto, H. Kishihara, R. Kubo, T. Usuki, M. Okuyama, *Sens. Mater.*, **12**, 375 (2000).
- [3] X. Chen, W. Zhu, O. Tan, *Mater. Sci. Eng. B* **77**, 177 (2000).
- [4] I. Vendik, O. Vendik, V. Pleskachev, M. Nikol'ski, *IEEE Trans. Appl. Supercond.* **13**(2), Part 1, 716 (2003).
- [5] S. W. Kirchoefer, E. J. Cukauskas, N. S. Barker, H. S. Newman, W. Chang, *Appl. Phys. Lett.* **80**(7), 1255 (2002).
- [6] V. Vinothini, Paramanard Sigh, M. Balasubramanian., *Ceramics International.* **32**(99), 99 (2006).
- [7] Ken-ichi Mimura, Toshinobu Yogo, *Journal of the Ceramic Society of Japan.* **119**, 776 (2011).
- [8] A. S. Shaikh, G. M. Vest, *J. Am. Ceram. Soci.* **69**, 682 (1986).
- [9] M. Boulos, S. Fritsch, F. Mathieu, B. Durand, T. Lebey, V. Bley, *Solid State Ionics.* **176**(13), 1301-1309.
- [10] U. Manzoor, D. K. Kim, *J. Mater. Sci. Technol.* **23**(5), 655 (2007).
- [11] L. V. Maneeshya, V. S. Anitha, S. Sujatha Lekshmy, I. John Berlin Prabitha, B. Nair Georgi, P. Daniel, P. V Thomas, K. Joy, *J. Mater Sci: Mater Electron.* **24**, 848 (2013).
- [12] S. Vineet Dharmadhikari, W. W. Grannemann, *J. Appl. Phys.* **53**, 8988 (1982).
- [13] P. Bhattacharya, T. Komeda, D. Park, Y. Nishioka, *J. Appl. Phys.* **32**, 4103(1993).
- [14] D. Tahan, A. Safari, L. C Klin, *J. Am. Ceram. Soci.* **79**, 1593 (1996).
- [15] A. Abdel Aal, M. M. Rashad, G. A. Amin, *Journal of Physics: Conference Series* **61**, 1 (2007).
- [16] Z. M. Huang, Z. H. Zhang, C. P. Jiang, J. Yu, J. L. Sun, J. H. Chu, *Appl. Phys. Lett.* **77**, 3651(2000).
- [17] Z. G. Hu, G. S. Wang, Z. M. Huang, X. J. Meng, Q. Zhao, J. H. Chu, *Appl. Phys. A*(2003) (DOI: 10.1007/s00339-002-2043-y).
- [18] Begg, Bruce D., Vance, Eric R., Nowotny, Janusz, j. *Am. Ceram. Society*, **77**, 3186 (1994).
- [19] B. D. Stojannovic, A. Z. Simoes, C. O. Paiva – santos, j. *Eur. Ceram. Soc.* **25**, 1985 (2005).
- [20] S. Wada, M. Narahata, T. Hoshina, *J. Mater. Sci.* **38**, 2655 (2003).
- [21] S. Kribalis, P. E. Tsakiridis, C. Dedeloudis, E. Hristoforou, *J. Optoelectron. Adv. Matter.* **8**(4), 1475 (2006).
- [22] T. Mahalingam, V. S. John, G. Ravi, P. J. Sebastian, *Cryst. Res. Technol.* **37**, 329 (2002).
- [23] M. Sridharan, Sa. K. Narayandass, D. Mangalaraj, H. C. Lee, *Cryst. Res. Technol.* **37**, 964 (2002).
- [24] S. H. Jeong, S. Kho, D. Jung, S. B. Lee, J. H. Boo, *Surface and Coatings Technology* **187**, 174 (2003).
- [25] K. K. Chattopadhyay, A. Sarkar, S. Chaudhuri, A. K.

- Pal, Vacuum. **42**(17), 1113 (1991).
- [26] C. A. Neugebauer, M. B. Webb, J. Appl. Phys. (USA). **33**, 74 (1962).
- [27] R. Sengodan, B. Chandar shekar, S. Sathish, J. Optoelectron. Adv. Matter. **14**(7- 8), 653 (2012).
- [28] Z. G. Hu, G. S. Wang, Z. M. Huang, J. H. Chu, J. Phys. Chems. sol. **64**, 2445 (2003).
- [29] R. Thomas, D. C. Dube, M. N. Kamalasanan, S. Chandra, Thin Solid Films **346**, 212 (1999).
- [30] E. Saryga, J. Swiatek, Thin Solid Films. **56**, 311 (1979).
- [31] J. Swiatek, Phys. Stat. Sol. A. **38**, 285 (1976).
- [32] P. Li, T. M. Lu, phys. Rev. B. **43**, 14261 (1991).
- [33] E. Saryga, J. Swiatek, Thin Solid Films, **56**, 311 (1979).
- [34] ReJi Thomas, D. C. Dube, M. N. Kamalasanan, N. Deepak Kumar, J. Sol – Gel. Sci. Tech. **16**, 101 (1999).

*Corresponding author: chandar.bellan@gmail.com